Journal of
*Manufacturing and Materials Processing*

MDPI

*Article*

# Microstructure Refinement of Bulk Inconel 718 Parts During Fabrication with EB-PBF Using Scanning Strategies: Transition from Bidirectional-Raster to Stochastic Point-Based Melting

**Shadman Tahsin Nabil [1,2,*], Cristian Banuelos [1,2], Michael E. Madigan [3], Sammy Tin [3], Jacob I. Rodriguez [1,2], Lawrence E. Murr [1,4], Ryan B. Wicker [1,2] and Francisco Medina [1,2]**

[1] W.M Keck Center for 3D Innovation, University of Texas at El Paso, El Paso, TX 79968, USA
[2] Department of Aerospace and Mechanical Engineering, University of Texas at El Paso, El Paso, TX 79968, USA
[3] Department of Materials Science and Engineering, University of Arizona, Tucson, AZ 85719, USA
[4] Department of Metallurgical, Materials and Biomedical Engineering, University of Texas at El Paso, El Paso, TX 79968, USA
* Correspondence: snabil@miners.utep.com

**Abstract:** Inconel 718 is a widely popular aerospace superalloy known for its high-temperature performance and resistance to oxidation, creep, and corrosion. Traditional manufacturing methods, like casting and powder metallurgy, face challenges with intricate shapes that can result in porosity and uniformity issues. On the other hand, Additive Manufacturing (AM) techniques such as Powder Bed Fusion (PBF) and Direct Energy Deposition (DED) can allow the creation of intricate single-part components to reduce weight and maintain structural integrity. However, AM parts often exhibit directional solidification, leading to anisotropic properties and potential crack propagation sites. To address this, post-processing treatments like HIP and heat treatment are necessary. This study explores the effects of the raster and stochastic spot melt scanning strategies on the microstructural and mechanical properties of IN718 parts fabricated using Electron Beam Powder Bed Fusion (EB-PBF). This research demonstrates that raster scanning produces columnar grains with higher mean aspect ratios. Stochastic spot melt scanning facilitates the formation of equiaxed grains, which enhances microstructural refinement and lowers anisotropy. The highest microstructural values were recorded in the raster-produced columnar grain structure. Conversely, the stochastic melt-produced transition from columnar to equiaxed grain structure demonstrated increased hardness with decreasing grain size; however, the hardness of the smallest equiaxed grain structure was slightly less than that of the columnar grain structure. These findings underscore the vital importance of scanning strategies in optimizing the EB-PBF process to enhance material properties.

**Keywords:** microstructure control; electron beam melting; scanning strategy; Inconel 718; spot melting



**Citation:** Nabil, S.T.; Banuelos, C.; Madigan, M.E.; Tin, S.; Rodriguez, J.I.; Murr, L.E.; Wicker, R.B.; Medina, F. Microstructure Refinement of Bulk Inconel 718 Parts During Fabrication with EB-PBF Using Scanning Strategies: Transition from Bidirectional-Raster to Stochastic Point-Based Melting. *J. Manuf. Mater. Process.* **2024**, *8*, 241. https://doi.org/10.3390/jmmp8060241

Academic Editors: Hamed Asgari and Elham Mirkoohi

Received: 25 September 2024
Revised: 27 October 2024
Accepted: 28 October 2024
Published: 31 October 2024



## 1. Introduction

Metal additive manufacturing (AM) has transformed the modern aerospace and defense sectors [1–3]. This manufacturing approach has been widely adopted and suited for manufacturing of aerospace alloys such as aluminum and nickel-based superalloys to produce operational components [4–6]. AM technologies like powder bed fusion (PBF), direct energy deposition (DED), and binder jetting have allowed the possibility of producing single-part components while substantially reducing weight without compromising structural integrity [7–9].

Inconel 718 is a widely used nickel-based superalloy. It is a precipitation-hardened alloy and can retain strength at elevated temperatures up to 650 °C. It comprises primarily 50–55% nickel and 17–21% chromium, alongside 4.8–5.5% niobium, 2.8–3% molybdenum, 0.65–1.15% titanium, and 1% cobalt, with iron and aluminum constituting the

balance [10,11]. This alloy exhibits an excellent combination of resistance to creep, oxidation, and corrosion, making it suitable for aerospace applications and sectors, including aircraft, gas turbine engines, rocket engines, valves, flow control devices, turbine blades, etc. [12].

Traditional manufacturing processes like casting and powder metallurgy have been proven effective in producing functional components of Inconel 718 [12–14]. However, due to the nature of the alloy, these methods face challenges during complex geometry fabrication, including issues like porosity from entrapped gas during casting, and issues with sintering during powder metallurgy processes [13,15]. Moreover, these parts require extensive subtractive techniques after fabrication to achieve working parts with structural integrity [16]. Nowadays, advances in computer-aided design software, particularly through topology optimization and generative designs, allow for the transformation of multiple parts into a single, more efficient component with significant weight reduction [17]. Navigating the complexities of intricate geometries presents considerable challenges; however, additive manufacturing stands out as a solution to effectively address these difficulties [18].

One of the major issues with AM-fabricated parts is directional solidification in the build direction, leading to epitaxial grain growth along the build direction [19–21]. Such microstructural variations significantly influence the mechanical properties, deviating from those produced through conventional processes [22,23]. Additionally, these epitaxial boundaries can become preferential sites for crack propagation [24,25]. As a result, parts produced through AM require post-processing treatments like hot isostatic pressing (HIP) and heat treatment (HT) to meet necessary application standards [26,27]. Both DED and PBF technologies are employed in the aerospace industry to fabricate IN718 parts, with PBF being particularly popular for producing complete components from this alloy.

Electron Beam Powder Bed Fusion (EB-PBF) is a Powder Bed Fusion (PBF) technology that uses an accelerated electron beam, which is directed at high velocity to selectively melt metal powder, layer by layer, for part fabrication [28]. In an EB-PBF machine, the entire chamber is maintained under vacuum conditions. One distinctive feature of EB-PBF is that it operates as a hot working process; the parts are fabricated inside the vacuum chamber at elevated temperatures, and typically the build plate is heated around 0.80 of the material's melting temperature ($T_m$). This approach reduces thermal stresses in the melted parts, and stress relief occurs during the cooling phase of part fabrication [29].

The electron beam's path during the melting of powders is termed a scanning strategy. The most common scanning strategy in EB-PBF is the bidirectional raster snake melt scan, where the melt scanning pattern moves in lines, and the key parameters are spot size, speed, and power [30,31]. There is another scanning strategy that utilizes beam spots instead of lines, with key parameters including spot size, spot dwell time, and power [32–34].

Previous studies done with raster scans on EB-PBF for IN718 fabrication showed directional solidification with columnar grains in the build direction [35–38]. To minimize this anisotropy, some research has explored rotating the raster scan layer by layer in builds, which has been observed to minimize epitaxial growth during the build process [39,40]. Additionally, research employing an offset method to control the microstructure in IN718 fabrication has demonstrated that defects in the build direction can restrict directional solidification and promote the formation of equiaxed grains [41]. Moreover, some point-based spot melt techniques showed possibilities for columnar to the equiaxed transformation of grains [21,32,42,43]. The research established that controlling temperature gradient (G), increasing solidification rate (R), and creating restrictions at the solidification front can allow the formation of equiaxed dendritic growth in the microstructure [44–46].

Figure 1 provides a detailed solidification map explanation with temperature gradient (G) and solidification rate (R) adapted from the welding metallurgy process [47]. The diagram showcases the effect of G and R on the solidification structure of metals. It highlights that lowering the temperature gradient and increasing the growth rate R promotes the formation of equiaxed grains over columnar grains, leading to a more significant columnar to equiaxed grain transformation (CET).

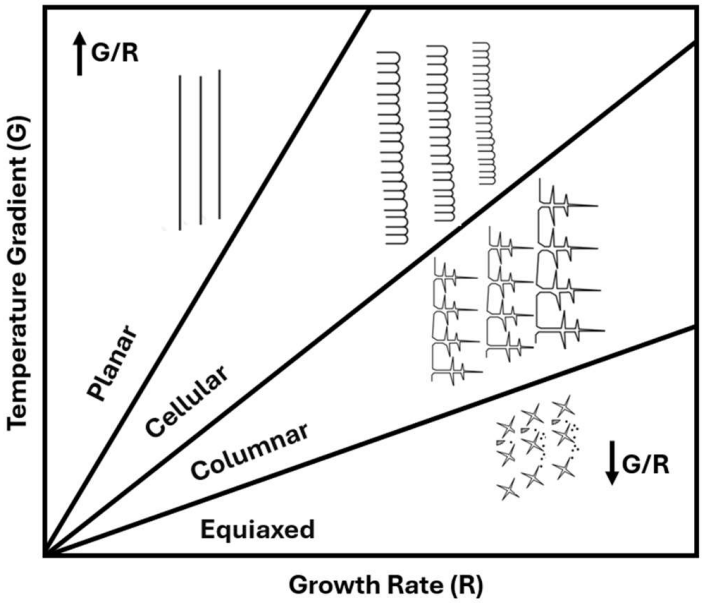


**Figure 1.** Relation between temperature gradient (G) and growth rate (R) in microstructure formation—adapted from [47].

The current research explores raster and stochastic spot melt scanning strategies to build bulk IN718 parts. The primary goal is to promote grain refinement by affecting meltpool dynamics using stochastic spot melt and compare it with raster builds. The objective is to lower the mean aspect ratio—denoted as microstructure refinement—thus minimizing anisotropy. The research begins with process optimization for both techniques for the dense build, followed by electron backscattered diffraction (EBSD) evaluation and comparing hardness values to provide an overall impact of scanning strategies in the microstructure and performance.

## 2. Materials and Methods

### *2.1. Powder Characteristics*

This study utilized plasma-atomized spherical powder from AP&C IN718. The powder size distribution ranged between 45 and 106 µm, with corresponding values for D10, D50, and D90 being 52 µm, 73 µm, and 105 µm, respectively. The flowability measure was 11 s/50 g. The powder was reused multiple times after proper sieving for the fabrication.

### *2.2. Fabrication Process*

An open-source EB-PBF machine, FreemeltOne (Freemelt AB, Mölndal, Sweden), was used for solid part fabrication. The print process in FreemeltOne EB-PBF is divided into four stages: start heat, preheat, melt, and post-heat, which are executed sequentially in each cycle during printing. During its run time, the machine operates in a high vacuum in the range of $10^{-5}$ and $10^{-6}$ torr.

In each build, the build plate was heated up to 1050 °C as a startheat function. Following this, two custom scan preheat strategies were employed—rectangular preheat scan for raster melt and circular preheat scan with bezier curves for spot melt. These customs preheat strategies were created using the OBPLIB function in a Python library. Before the beginning of the build, the cathode was calibrated with a beam calibration function where the spot size at 1% corresponded to a 0.265 mm beam diameter, and 150% corresponded to a 1.2 mm beam diameter. For preheating, a maximum spot size (150%) or defocused beam was used for part fabrication, and a 1% spot size was used for the melt to ensure proper fusion of the powders. Figure 2 represents the adopted preheat strategies for both builds. The distance from each beam path was increased to 1.2 mm (termed line offset) to ensure

enough distance so that the powders could retain the heat without getting overly sintered and minimize smoke events. Additionally, the lines or curves were shifted in a way so that there was no overlap between each.

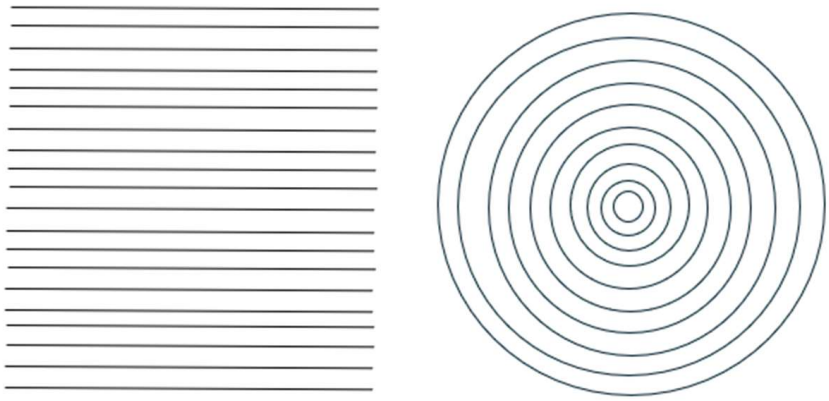

(**a**) (**b**)

**Figure 2.** Preheat strategies implemented during build; (**a**) raster build; (**b**) spot melt build.

The melt process was explored employing two different scanning strategies—one with a bidirectional raster scan method and another with a randomized spot melt method. Figure 3 represents the scanning melt strategy implemented in this research work. The distance between two consecutive raster lines and points was kept at 0.1 mm for melt. Based on powder distribution, the layer height was maintained at 75 microns.

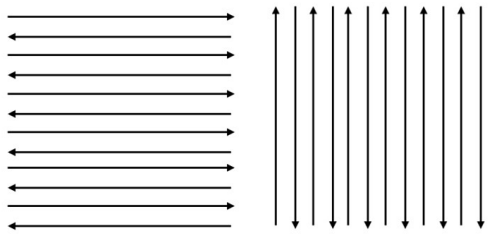


(**a**) Bidirectional raster scanning strategy (N and N+1 layers).

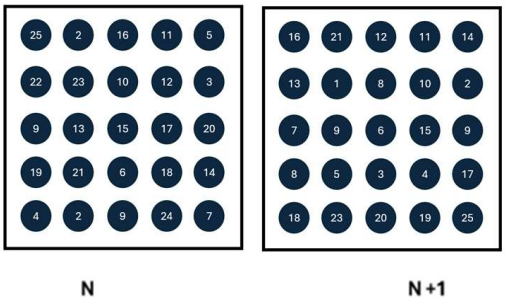


(**b**) Stochastic spot melt scanning strategy (N and N+1) layers.

**Figure 3.** Scan strategies implemented during the build; (**a**) raster build; (**b**) stochastic spot melt.

A heuristic design approach was followed for all of the DOE parameter development. This was used to develop the parameters to achieve dense builds. The optical density of the builds was assessed using ImageJ software. It was done by converting polished surface images to 8-bit grayscale and applying a threshold where the porous regions appeared black, and the solid areas were white. This method allowed for the measurement of the dense material by calculating the area covered by the white regions, which was then used to determine the relative density based on the ratio of dense (white) to porous (black) areas.

In the raster scanning method, the pattern implemented was bidirectional raster, as shown in Figure 3a, and the evaluated build geometries were 20 mm × 20 mm × 10 mm cuboids, as shown in the left of Figure 4a. Once a solid dense build (>99% relative optical density) was achieved with optimized parameters as shown in Figure 4a, center 15 mm × 15 mm × 30 mm cuboids (Figure 4a, right) were built for the verification build.

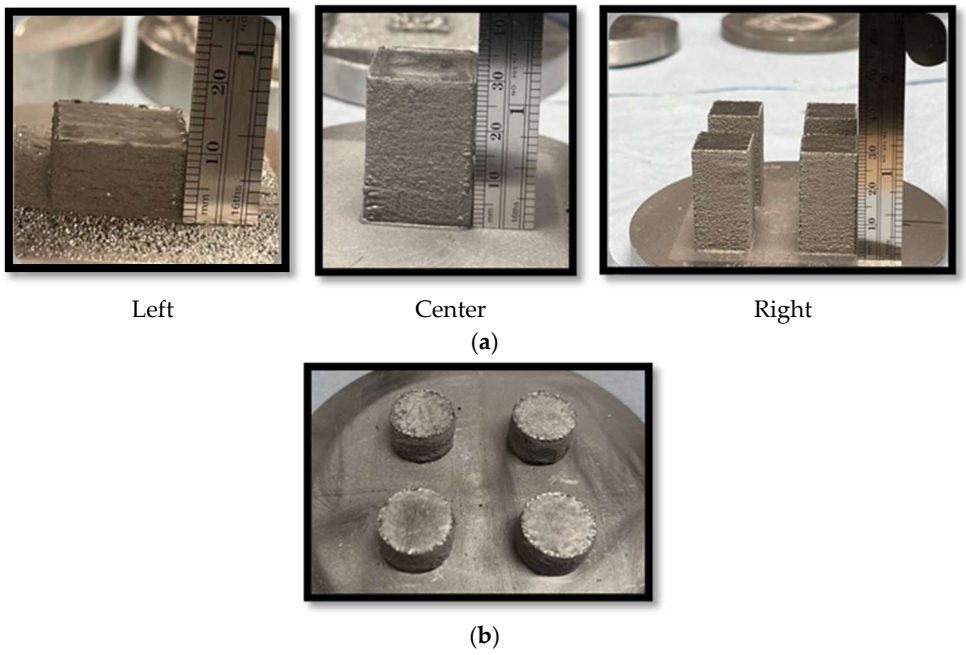


**Figure 4.** Build fabrication process for (**a**) raster build and (**b**) stochastic spot melt build.

An open-source Python library, OBPLIB, created by (Freemelt AB, Sweden) was used to make the bidirectional beam pattern for raster builds. In this scanning method, the beams change direction like a snake with each subsequent scan line. The beam does not turn, but is briefly turned off before shifting to the raster scan line.

For the spot melt method, randomized controlled point melt (stated as stochastic spot melt) was implemented using PixelMelt Cloud Software (Freemelt AB, Sweden). The build geometry for spot melt was 15 mm diameter cylinders with 10 mm height, as shown in Figure 4b. The choice of geometry kept cylinders to ensure easier removal of sintered powder, and since both cuboids and cylinders were bulk parts, primary analysis showed no variation in the results. Four builds with different parameters were evaluated in one go. This randomized point melt converts the 2D print area into a small mesh (0.1 mm × 0.1 mm) and takes each center of the mesh as a point of melt. For each subsequent layer, the distribution of which point to choose for melt inside the mesh is randomized, as demonstrated in Figure 3b. Neighborhood cooling—an option in the software—was turned on to minimize the remelting of the points from previous layers in the ongoing layer.

Equation (1) shows the energy density for raster melt as Energy per Area ($E_a$), and Equation (2) shows the energy density for spot melt as Energy per Area Spot ($E_{as}$) [43].

$$E_a = \frac{P}{v_b \times h_s} \quad (1)$$

The raster melt energy density ($E_a$) represents the energy delivered per unit area. During the raster melting process, an electron beam moves continuously along parallel tracks and melts the material layer by layer. The energy delivered depends on the beam power ($P$), the beam speed ($V_b$), and the hatch spacing ($h_s$), which is the distance between adjacent tracks.

The energy density for spot melt ($E_{as}$) refers to the energy delivered per unit area. During spot melt, the beam melts discrete points instead of moving continuously. The energy density for spot melt is defined by the beam power ($P$), the beam on-time or dwell time ($t_{on}$), and the spacing between adjacent spot melts ($S_s$).

$$E_{as} = \frac{P \times t_{on}}{s_s^2} \quad (2)$$

### 2.3. Microstructure and Hardness Characterization

The microstructure of the builds was evaluated using Electron Backscatter Diffraction (EBSD) on a Tescan Mira 3 Scanning Electron Microscope (SEM). Four different parameter sets of stochastic spot melt prints were assessed through EBSD characterization and compared with the EBSD data obtained parallel to the build direction for the raster builds. Microhardness measurements were conducted on the samples using a QATM CHD Master Microhardness tester on the HV1 scale following ASTM E384-17. The indentations are made diagonally along the plane parallel to the build direction.

## 3. Results and Discussion

### 3.1. Parameter Development

The parameter development process was split into two parts: one for the raster scan-build and one for the stochastic spot melt build.

For the raster parameter development, the energy density, $E_a$, was kept between 2.5 and 3.75 J/mm$^2$. Variations of power and speed were experimented with during this process. Table 1 represents the successful builds from the experimentation process with respect to their optical relative density. Builds that appeared dense upon visual analysis were classified as "Solid" in Table 1, while those showing a lack of fusion (LOF) in optical image analysis were classified as "LOF". Lower speed and lower power facilitated a stable melt pool, resulting in a higher-density build.

**Table 1.** Experimental parameters for raster scan builds.

| Power (W) | Speed (mm/s) | $E_a$ (J/mm$^2$) | Relative Optical Density (%) | Type |
|---|---|---|---|---|
| 720 | 2400 | 3 | 97.81 | Solid |
| 600 | 2400 | 2.5 | 95.7 | LOF |
| 300 | 1200 | 2.5 | 96.47 | LOF |
| 360 | 1200 | 3 | 98.38 | Solid |
| 300 | 800 | 3.75 | 99.87 | Solid |

For stochastic spot scan, a large range of $E_{as}$, energy per spot area, was explored between 5.8 and 16.9 J/mm$^2$, as shown in Figure 5. It was explored to evaluate the effect of different power and dwell time in the optical relative density of parts. The samples that had lack of fusion was labeled LOF, looked solid, was labeled Solid, and had swelling after the build due to excessive energy, and was labeled as Swell. $E_{as}$ in the range of 9 J/mm$^2$ to 10.5 J/mm$^2$ had overall solid dense builds compared to others, as shown in Figure 5. It has been observed that the parts with identical $E_{as}$ had higher density when they were built with lower power and higher spot dwell time.

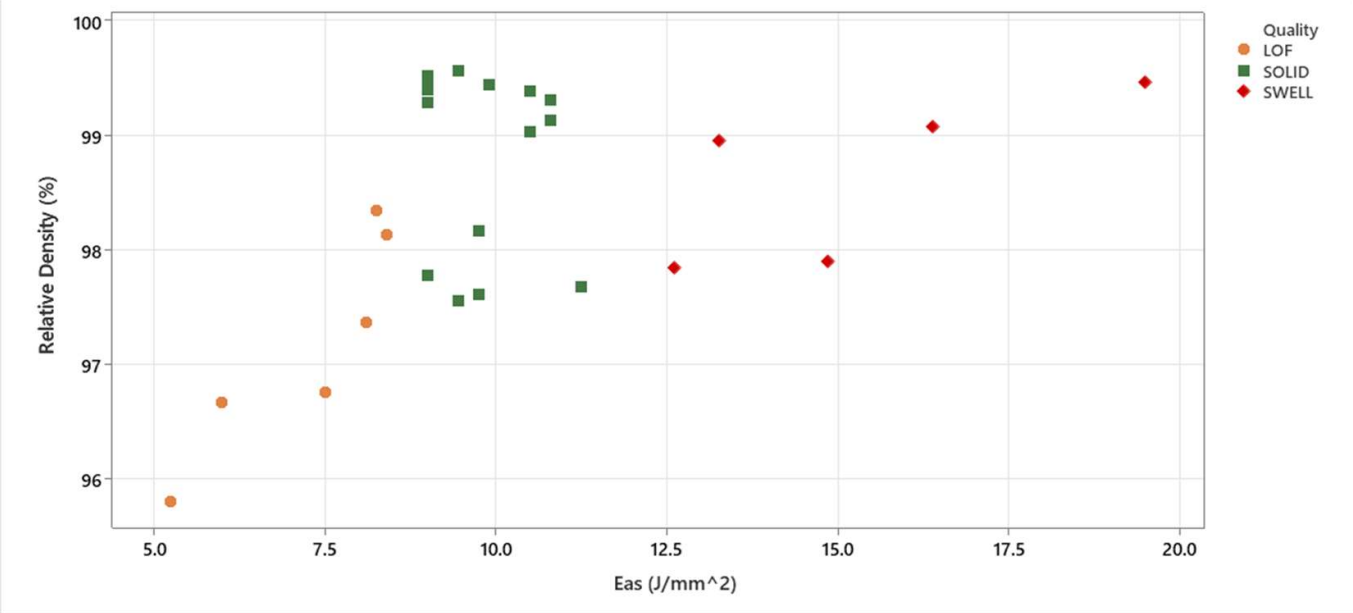


**Figure 5.** Scatterplot of relative density and energy $E_{as}$ for stochastic spot melt scan builds.

### *3.2. Microstructure Characterization*

#### 3.2.1. Raster Scan Build

The 30 mm height sample was used for the EBSD in the build direction (BD) and performed at the top and bottom sides, as demonstrated in Figure 6. Figure 6a,b represents the top and bottom in terms of the build height of the fabricated sample.

Both raster top and bottom exhibit columnar grain formation in build direction Z due to directional solidification. The top section in Figure 6a exhibits a more uniform grain orientation, predominantly [001] observed from the IPF coloring map. The bottom section in Figure 6b also exhibits [001] orientation with greater variability of grain orientation. This variability can be caused by the initial thermal gradient and solidification dynamics at the beginning of the print. At the initial build layers, the thermal gradient was low. This allowed grains to nucleate with some variation in orientation. The bidirectional scanning pattern also influenced localized thermal shifts, and affected grains to grow in slightly different directions as they formed. However, as layers build up, heat accumulates, creating a steeper thermal gradient over time. This increased thermal gradient drives more directional solidification, encouraging grain growth to align increasingly along the build direction and producing a more consistent columnar grain structure in the upper layers.

Figure 6c,d further illustrates the crystallographic texture in both sections. It is observed that both sections exhibit a strong <100> texture component, but with differences in orientation clustering. The pole figures corresponding to the top section show concentrated intensity peaks, indicating a stronger and more uniform crystallographic texture. In contrast, the pole figures for the bottom display slightly more dispersed peaks, suggesting greater variability in orientation.

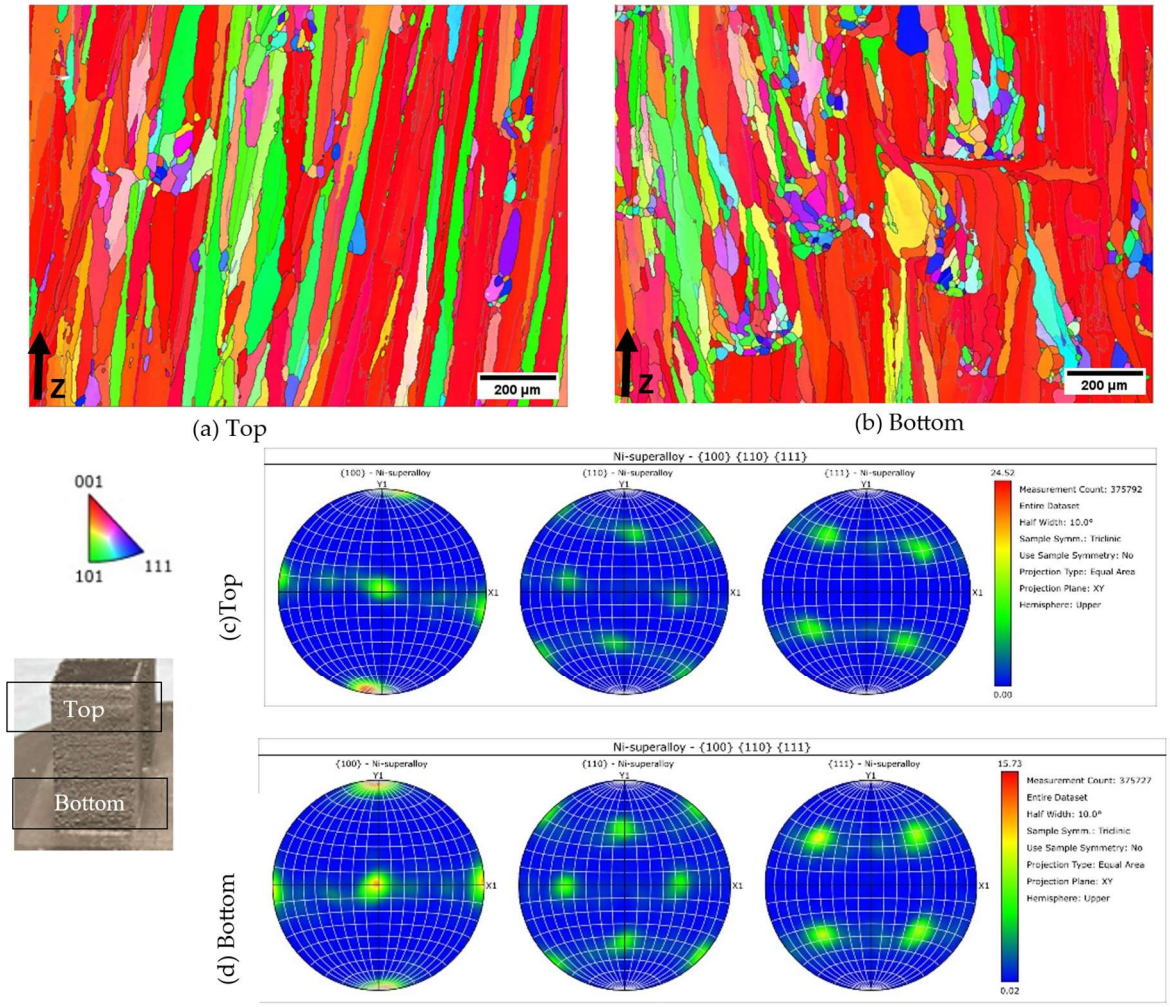


**Figure 6.** EBSD results for raster scan build; (**a**) top; (**b**) bottom; and pole configuration (**c**) top; (**d**) bottom of the build specimen in the build direction.

### 3.2.2. Stochastic Spot Scan Build

Four individual samples from the stochastic spot builds were chosen to observe for EBSD to evaluate the impact of power and spot dwell in the microstructure of the build direction. The $E_{as}$ varied in these samples between 8.25 and 10.25 J/mm$^2$. Table 2 shows the samples that were evaluated. Samples were done EBSD, parallel to the build direction (parallel to rake movement) and perpendicular to the build direction, as shown in Figure 7.

**Table 2.** EBSD specimens evaluated for stochastic spot melt.

| Specimen | SP1 | SP2 | SP3 | SP4 |
|---|---|---|---|---|
| Power (Watt) | 720 | 660 | 420 | 360 |
| Spot Dwell (microseconds) | 125 | 125 | 250 | 250 |
| $E_{as}$ (J/mm$^2$) | 9 | 8.25 | 10.25 | 9 |
| Melt Time (seconds) | 2.21 | 2.21 | 4.42 | 4.42 |

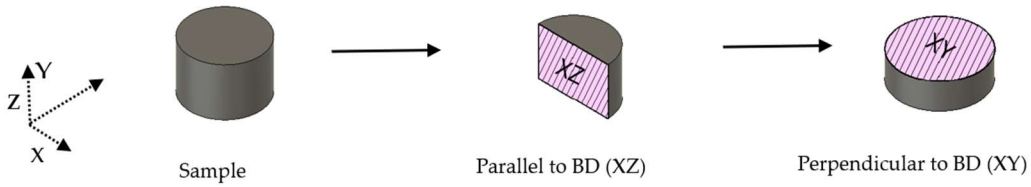


**Figure 7.** Schematic diagram illustrating sample direction and assessment method.

Figures 8 and 9 show EBSD results perpendicular and parallel to the build direction, respectively. Upon observation, EBSD results perpendicular to the build direction (Figure 8) showed no significant microstructure variations. As the observation was from the top (XY plane), they exhibited equiaxed grains. In addition, it was also seen that SP1 and SP2 had larger grain sizes than SP3 and SP4 upon naked observation.

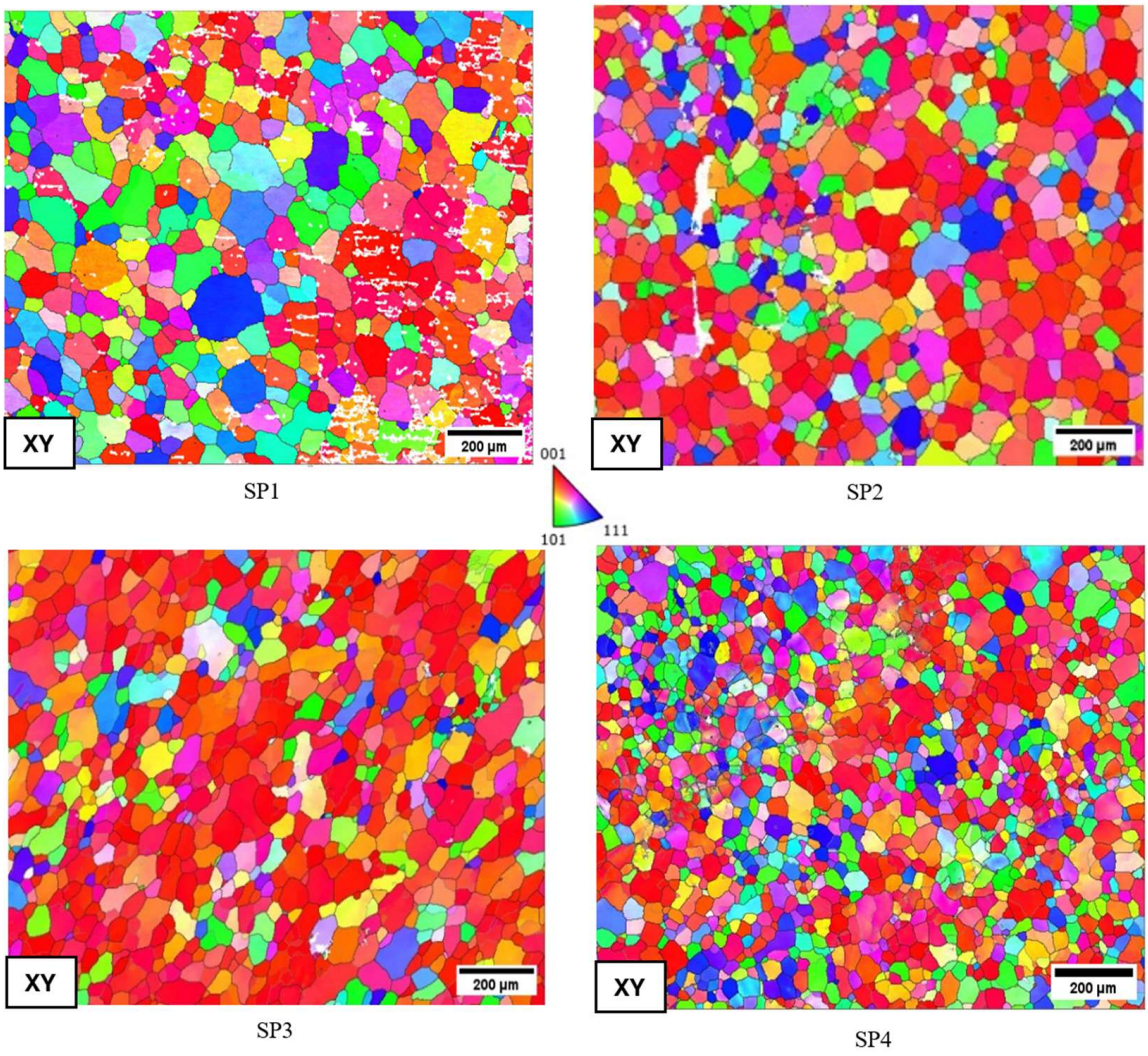


**Figure 8.** EBSD results for spot melt specimens perpendicular to build direction.

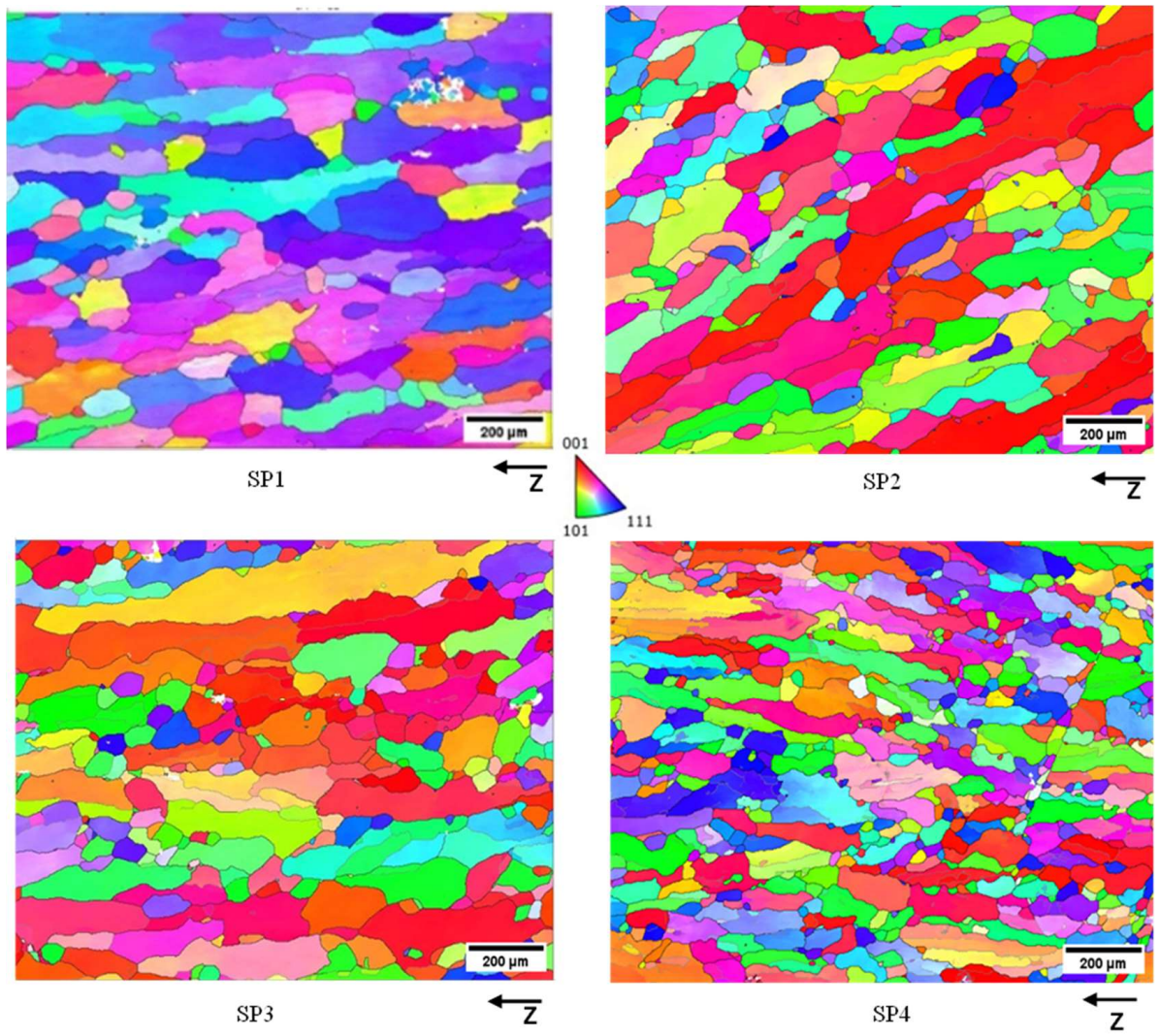


**Figure 9.** EBSD results in parallel to build direction for stochastic spot melt samples.

On the other hand, the EBSD result parallel to the build direction in the XZ plane (Figure 9) shows more significant variation in microstructures, denoting columnar to equiaxed transformation (CET) from the SP1 to SP4 samples. In the SP1 sample, the EBSD map showed dominant elongation of grains with fewer equiaxed grains. In SP2, similar characteristics of elongated grains were observed, as some grains appeared smaller than SP1. This indicated microstructural refinement as we lowered the power from SP1 to SP2 while maintaining the same dwell time.

Furthermore, the SP3 EBSD map showed a transition to a more refined grain by being less elongated and more equiaxed. Lower power and higher dwell time showed further grain refinement and CET introduction. Finally, In SP4 samples, further lowering the power and keeping a higher dwell time resulted in a more refined grain structure with prominent uniform grains and fewer elongated grains, resulting in a successful CET transformation.

Figures 10 and 11 show pole configuration for SP1 to SP4 samples in perpendicular and parallel directions. The pole configurations perpendicular to the build direction (Figure 9) show typical pole configurations similar to equiaxed grain and were consistent across all the samples.

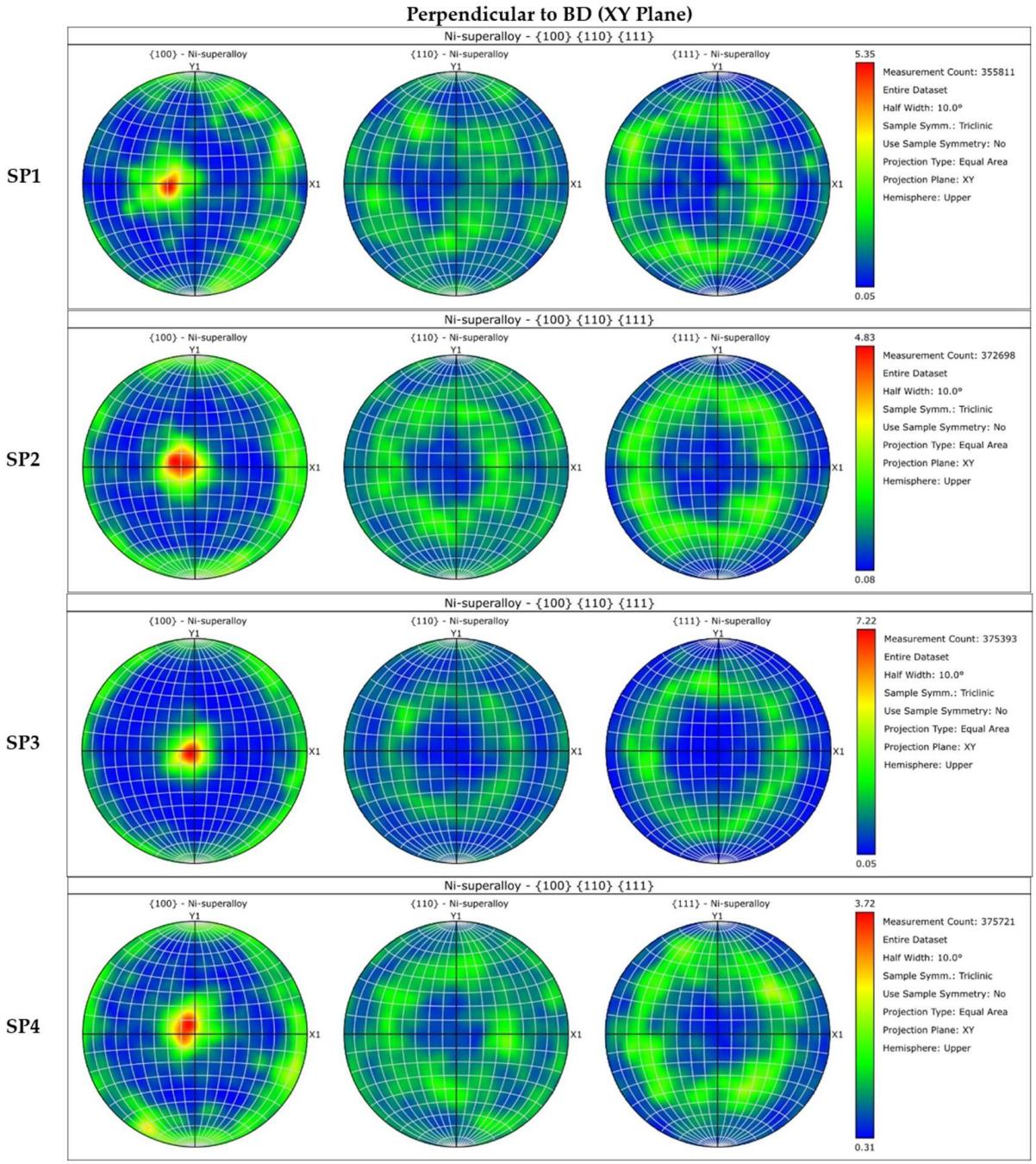


**Figure 10.** Pole configuration of the EBSD samples perpendicular to the build direction.

In SP1, pole density is concentrated and shows the early stages of CET transformation. Followed by that, in SP2 and SP3, increased and diffused densities in the <100>, <110>, and <111> pole configurations are observed. In SP4, the pole configuration exhibited the highest diffusion, indicating further refinement and progression to CET transformation.

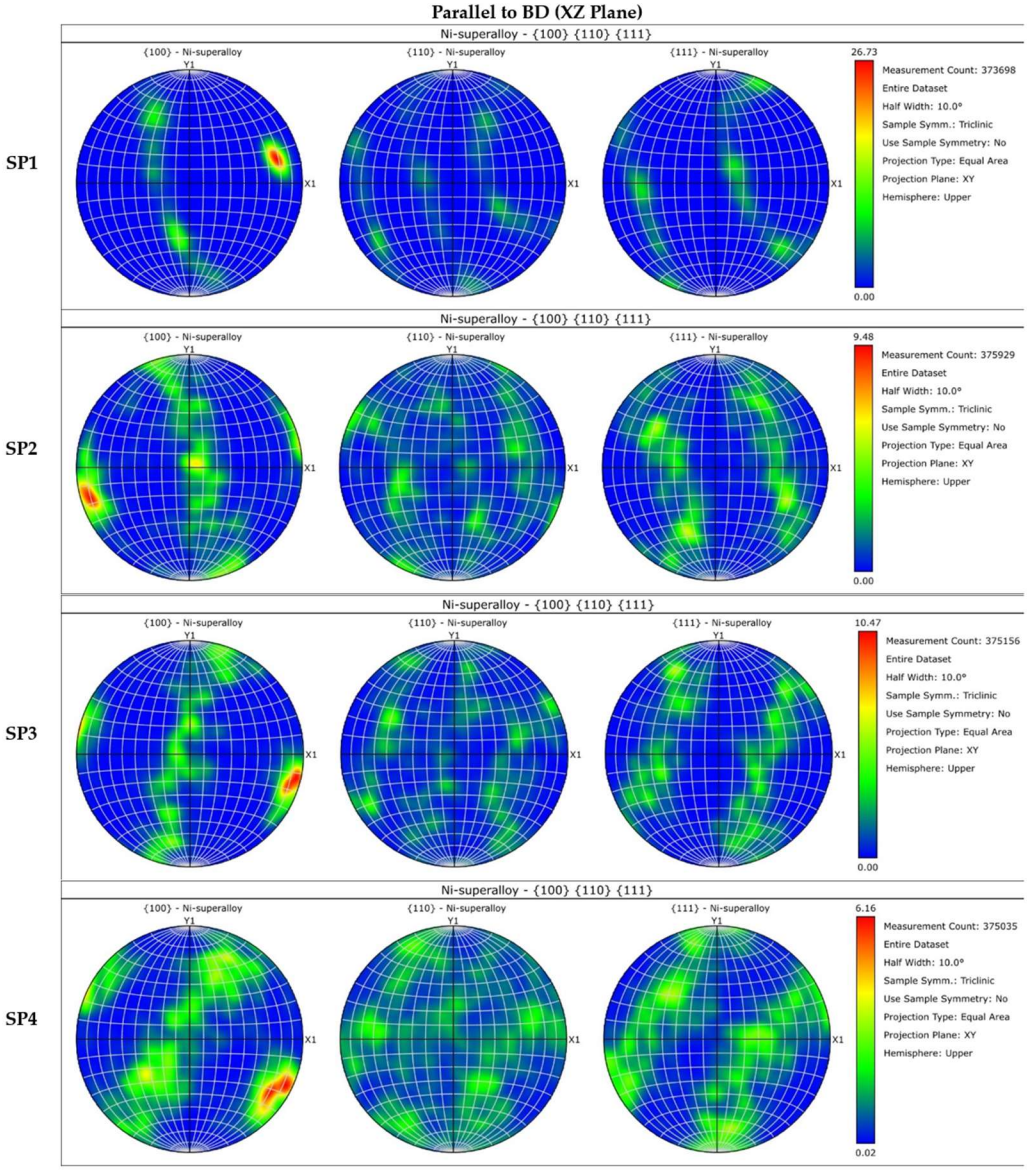


**Figure 11.** Pole configuration of the EBSD samples parallel to the build direction.

In Table 2, both SP1 and SP2 had identical dwell times of 2.21 s. These similar melt times allowed consistent thermal exposures and resulted in identical microstructural features. Lowering the melt power in this situation stabilized further heat distribution within the melt pool and showed increased promotion of CET in SP2. In SP3 and SP4, the dwell time was doubled to 4.42 s. In these cases, higher melt time was attributed to superior heat distribution within the melt pool, and lowering the power allowed more CET transformation in SP4 samples.

### 3.2.3. Comparison Between Raster and Stochastic Spot Melt EBSD Results

Table 3 shows the comparative EBSD data of all the build samples parallel to the build direction (XZ). Upon observation, the raster build shows a greater grain count at the bottom (813) because of a lower thermal gradient at the beginning, which lowered at the top (425) due to an increased thermal gradient. On the other hand, from SP1 to SP4, a consistent increase in grain count was observed from 192 to 6433.1.

**Table 3.** Detailed observations from EBSD results for raster and stochastic spot melt build.

| Metric (Parallel to Build Direction) | Raster Build | | Stochastic Spot Melt Build | | | |
|---|---|---|---|---|---|---|
| | Top Section | Bottom Section | SP1 | SP2 | SP3 | SP4 |
| Grain Count | 425 | 813 | 192 | 308 | 342 | 643 |
| Mean Aspect Ratio | 5.9 | 3.6 | 2.9 | 2.7 | 2.6 | 2.5 |
| Area-weighted Mean Aspect Ratio | 10.9 | 5.6 | 3.5 | 4.0 | 3.9 | 3.5 |
| Min Aspect Ratio | 1.1 | 1.0 | 1.0 | 1.1 | 1.0 | 1.0 |
| Max Aspect Ratio | 36.8 | 36.3 | 9.6 | 9.8 | 9.9 | 12.7 |
| Standard Deviation | 5.4 | 2.9 | 1.6 | 1.5 | 1.5 | 1.5 |

Observing the mean aspect ratio, the raster build had a mean aspect ratio of 3.6 at the bottom, which increased to 5.9 at the top. The area-weighted mean aspect ratio was also significantly higher for the raster at the top (10.9) compared to the bottom (5.6). For both the top and bottom, a minimum aspect ratio of almost 1.1 and a maximum aspect ratio of 36.3 indicates a larger columnar grain presence throughout the sample. A standard deviation of 5.4 at the top and 2.9 at the bottom states that a greater grain size variation was observed at the top due to thermal turbulence.

In contrast, while observing stochastic spot melt samples from SP1 to SP4, a gradual decrease in mean aspect ratio was observed from 2.9 in SP1 to 2.5 in SP4. This lowering trend suggests further refinement for CET. The minimum and maximum aspect ratio ranged from 1 to 12.7 in all the samples, suggesting fewer columnar grains than raster builds. The lower standard deviation around 1.5 for all the samples indicates a higher degree of grain refinement in spot melt samples.

### *3.3. Microhardness Value in HV1 Scale*

Figure 12 and Table 4 show Vickers microhardness values evaluated on the parallel plane in the build direction of the HV1 scale. The raster samples exhibited the highest mean hardness of 434 HV1, with a standard deviation of 11.9. This higher hardness correlates with the columnar grain structure shown in Figure 6, while the regular increase in hardness for the stochastic melt builds is shown in Figures 8 and 9 are due to the decrease in the grain size for the equiaxed grain structure. This increase in hardness with a corresponding reduction in the grain size in Figures 8 and 9 are represented by the corresponding increase in the grain count shown in Table 3. In this regard, the raster builds shown in Figure 6 exhibit a much higher grain count in both the top and bottom sections than the stochastic builds shown in Table 3 for SP1 to SP3, while the bottom section raster build grain count is 813 in contrast to the smaller count for SP4. This is consistent with the hardness trends shown in Figure 12.

**Table 4.** Vickers microhardness results in the HV1 scale for raster and stochastic spot melt.

| Build | Test 1 | Test 2 | Test 3 | Test 4 | Test 5 | Mean | Standard Deviation |
|---|---|---|---|---|---|---|---|
| Raster | 451 | 437 | 431 | 418 | 432 | 434 | 11.9 |
| SP1 | 397 | 266 | 235 | 238 | 352 | 298 | 72.9 |
| SP2 | 395 | 306 | 288 | 304 | 359 | 330 | 44.9 |
| SP3 | 391 | 365 | 359 | 388 | 405 | 382 | 17.1 |
| SP4 | 401 | 412 | 408 | 406 | 412 | 408 | 4.1 |

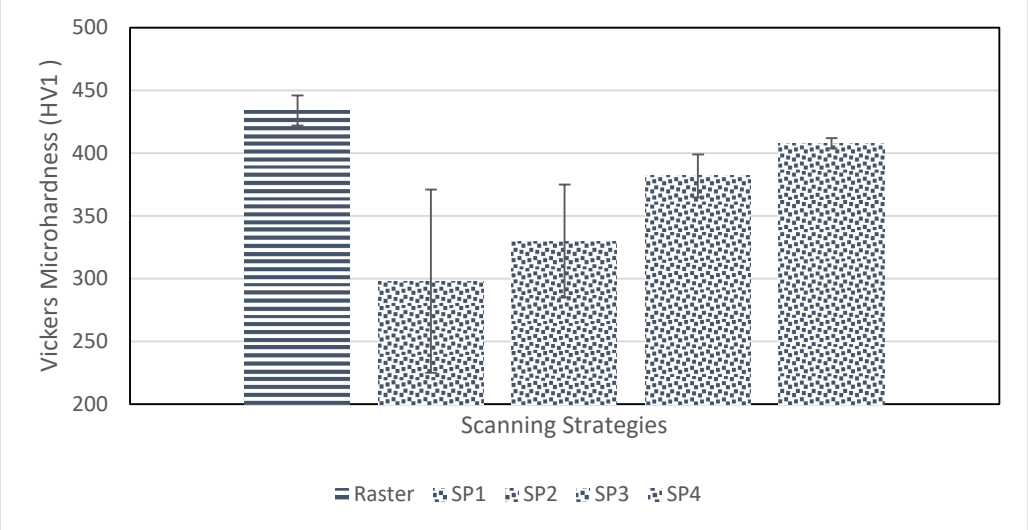


**Figure 12.** Vickers microhardness results in the HV1 scale for raster and stochastic.

On the other hand, stochastic spot melt samples from SP1 to SP4 showed lower hardness values overall than raster samples. In SP1, a more significant standard deviation (72.9 HV1) was observed with a mean hardness of 298. In SP2 to SP4, we saw a gradual increase in hardness value to 408 in SP4 and a gradual decrease in standard deviation to 4.1 in SP4. This increased hardness can be attributed to a gradual increase in grain count in Table 3 and refined microstructure.

## 4. Conclusions

This study evaluates two scanning strategies—raster and stochastic spot melt—and their effect on the microstructure and hardness properties of EB-PBF-fabricated IN718 superalloys. The parameter development phase identified the optimal condition for each scanning strategy for dense builds. Raster scan was observed to achieve a dense build with lower power and speed at identical energy per area, whereas, for stochastic spot melt, higher dwell time and lower power were observed to produce dense parts at an energy range of 9 to 10.25 J/mm$^2$. EBSD analysis revealed a columnar grain structure, where the [100] orientation was prominent in raster samples aligned in the build direction. On the other hand, stochastic spot melt samples showed higher distributions of <100>, <110>, and <111> oriented grains, consistent with an equiaxed grain structure. Vickers microhardness measurement further highlights these differences. Raster builds exhibited the highest hardness for the thin, columnar grains, while the stochastic melt samples exhibited lower hardness values, which increased with decreasing equiaxed grain sizes. From SP1 to SP3, a gradually higher hardness value and lower standard deviation were observed. SP4 showed the highest hardness value for stochastic spot melt and lower standard deviation, denoting a more isotropic grain formation with refined gains. These findings underscore the importance of scanning strategies during the fabrication process for microstructure formation, and highlight the potential for microstructure refinement through controlled scanning strategies in the EB-PBF process.

**Author Contributions:** S.T.N.: Writing—review and editing, writing—original draft, conceptualization, fabrication, analysis. C.B.: Writing—review and editing, analysis, fabrication. M.E.M.: EBSD characterization, writing—review and editing. S.T.: Writing—review and editing, supervision. J.I.R.: Sample characterization, writing—review and editing. L.E.M.: Writing—draft revision, Writing—review and editing, supervision. R.B.W.: Writing—review and editing, supervision. F.M.: Writing—review and editing, supervision, conceptualization. All authors have read and agreed to the published version of the manuscript.

**Funding:** This work is supported by a research grant from the National Science Foundation (NSF) under Grant Number 2117801.

**Data Availability Statement:** Data are contained within the article. Any additional data/data sets are available from the authors.

**Conflicts of Interest:** The authors declare that they have no known competing financial interests or personal relationships that could have appeared to influence the work reported in this paper.

## References


1. Blakey-Milner, B.; Gradl, P.; Snedden, G.; Brooks, M.; Pitot, J.; Lopez, E.; Leary, M.; Berto, F.; du Plessis, A. Metal Additive Manufacturing in Aerospace: A Review. *Mater. Des.* **2021**, *209*, 110008. [CrossRef]
2. Ghosh, A.; Naiyer, I.; Gogoi, B.; Goswami, K.M.; Sharma, D.; Kumar, H.; Panda, A.; Kumar, R.; Sahoo, A.K. Implementation of the Additive Manufacturing Technology towards Producing High-Performance Aerospace Components—A Review. *AIP Conf. Proc.* **2024**, *3007*, 100043. [CrossRef]
3. Pradeep, P.V.; Paul, A.; Paul, L.; Davim, J.P. Chapter 8—Application of Micro Machining and Additive Manufacturing Processes for Difficult-to-Cut Materials in Aerospace Industry—A Review. In *Modern Manufacturing Processes for Aircraft Materials*; Gürgen, S., Pruncu, C.I., Eds.; Elsevier: Amsterdam, The Netherlands, 2024; pp. 227–262, ISBN 978-0-323-95318-4.
4. Nabil, S.T.; Arrieta, E.; Wicker, R.B.; Benedict, M.; Medina, F. Effect of Thermal Aging in the Fatigue Life of Hot Isostatic Pressed AlSi10Mg Fabricated by Laser Powder Bed Fusion. In Proceedings of the 33th Annual International Solid Freeform Fabrication Symposium—An Additive Manufacturing Conference, Austin, TX, USA, 25–27 July 2022.
5. Diaz, J.C.; Watanabe, K.; Rubio, A.; De La Cruz, A.; Godinez, D.; Nabil, S.T.; Murr, L.E.; Wicker, R.B.; Arrieta, E.; Medina, F. Effect of Layer Thickness and Heat Treatment on Microstructure and Mechanical Properties of Alloy 625 Manufactured by Electron Beam Powder Bed Fusion. *Materials* **2022**, *15*, 7767. [CrossRef]
6. Babu, S.S.; Raghavan, N.; Raplee, J.; Foster, S.J.; Frederick, C.; Haines, M.; Dinwiddie, R.; Kirka, M.K.; Plotkowski, A.; Lee, Y.; et al. Additive Manufacturing of Nickel Superalloys: Opportunities for Innovation and Challenges Related to Qualification. *Metall. Mater. Trans. A* **2018**, *49*, 3764–3780. [CrossRef]
7. DebRoy, T.; Wei, H.L.; Zuback, J.S.; Mukherjee, T.; Elmer, J.W.; Milewski, J.O.; Beese, A.M.; Wilson-Heid, A.; De, A.; Zhang, W. Additive Manufacturing of Metallic Components—Process, Structure and Properties. *Prog. Mater. Sci.* **2018**, *92*, 112–224. [CrossRef]
8. Zaman, S.; Favela, S.; Herrera, N.E.; Gandara, A.; Molina, L.; Hassan, M.S.; Gomez, S.G.; Ramirez, J.E.M.; Mahmud, M.S.; Martinez, A.C.; et al. 3D Printing of Cyanate Ester Resins with Interpenetration Networks for Enhanced Thermal and Mechanical Properties. *J. Appl. Polym. Sci.* **2024**, *141*, e55423. [CrossRef]
9. Hassan, M.S.; Delgadillo, A.; Mahmud, M.S.; Munoz, J.; Zaman, S.; Gomez, S.G.; Marquez, C.; Ho, J.C.; Lin, Y. Additive Manufacturing of Carbon Fiber Reinforced Epoxy Thermoset with Improved Thermomechanical Properties. *J. Compos. Sci.* **2023**, *7*, 171. [CrossRef]
10. Zhang, P.; Gao, Y.; Zhang, J.; Yue, X.; Zhou, H.; Sun, Y. Inconel 718 Alloy Strengthening Mechanism and Fatigue Life of Microtexture-Induced Microjet Coupled with Cavifying Water Jet. *Vacuum* **2024**, *222*, 113060. [CrossRef]
11. Nabil, S.T.; Banuelos, C.; Ramirez, B.; Cruz, A.; Watanabe, K.I.; Arrieta, E.; Wicker, R.B.; Medina, F. Exploring IN718 Alloy Production with Bi-Directional Raster and Stochastic Spot Melting Techniques Using an Open-Source Electron Beam Melting System. In Proceedings of the 34th Annual International Solid Freeform Fabrication Symposium—An Additive Manufacturing Conference, Austin, TX, USA, 14–16 August 2023.
12. Pollock, T.M.; Tin, S. Nickel-Based Superalloys for Advanced Turbine Engines: Chemistry, Microstructure and Properties. *J. Propuls. Power* **2006**, *22*, 361–374. [CrossRef]
13. Das, N. Advances in Nickel-Based Cast Superalloys. *Trans. Indian Inst. Met.* **2010**, *63*, 265–274. [CrossRef]
14. Gessinger, G.H.; Bomford, M.J. Powder Metallurgy of Superalloys. *Int. Metall. Rev.* **1974**, *19*, 51–76. [CrossRef]
15. Frech, T.; Scholzen, P.; Schäflein, P.; Löpenhaus, C.; Kauffmann, P.; Klocke, F. Design for PM Challenges and Opportunities for Powder Metal Components in Transmission Technology. *Procedia CIRP* **2018**, *70*, 186–191. [CrossRef]
16. Mostafaei, A.; Ghiaasiaan, R.; Ho, I.-T.; Strayer, S.; Chang, K.-C.; Shamsaei, N.; Shao, S.; Paul, S.; Yeh, A.-C.; Tin, S.; et al. Additive Manufacturing of Nickel-Based Superalloys: A State-of-the-Art Review on Process-Structure-Defect-Property Relationship. *Prog. Mater. Sci.* **2023**, *136*, 101108. [CrossRef]
17. Kumaran, M.; Senthilkumar, V.; Sathies, T.; Justus Panicker, C.T. 6—Design and Topology Optimization for Additive Manufacturing of Multilayer (SS316L and AlSi10Mg) Piston. In *Advances in Metal Additive Manufacturing*; Salunkhe, S., Amancio-Filho, S.T., Davim, J.P., Eds.; Woodhead Publishing Reviews: Mechanical Engineering Series; Woodhead Publishing: Cambridge, UK, 2023; pp. 203–217, ISBN 978-0-323-91230-3.
18. Xiong, Y.; Tang, Y.; Zhou, Q.; Ma, Y.; Rosen, D.W. Intelligent Additive Manufacturing and Design: State of the Art and Future Perspectives. *Addit. Manuf.* **2022**, *59*, 103139. [CrossRef]
19. Murr, L.E.; Gaytan, S.M.; Ramirez, D.A.; Martinez, E.; Hernandez, J.; Amato, K.N.; Shindo, P.W.; Medina, F.R.; Wicker, R.B. Metal Fabrication by Additive Manufacturing Using Laser and Electron Beam Melting Technologies. *J. Mater. Sci. Technol.* **2012**, *28*, 1–14. [CrossRef]

20. Li, Q.; Li, X.-R.; Dong, B.-X.; Zhang, X.-L.; Shu, S.-L.; Qiu, F.; Zhang, L.-C.; Zhang, Z.-H. Metallurgy and Solidification Microstructure Control of Fusion-Based Additive Manufacturing Fabricated Metallic Alloys: A Review. *Acta Metall. Sin. Engl. Lett.* **2024**, *37*, 29–53. [CrossRef]
21. Lee, D.; Park, S.; Lee, C.-H.; Hong, H.-U.; Oh, J.; So, T.-Y.; Kim, W.-S.; Seo, D.; Han, J.; Ko, S.-H.; et al. Correlation between Microstructure and Mechanical Properties in Additively Manufactured Inconel 718 Superalloys with Low and High Electron Beam Currents. *J. Mater. Res. Technol.* **2024**, *28*, 2410–2419. [CrossRef]
22. Zinovieva, O.; Zinoviev, A.; Ploshikhin, V. Three-Dimensional Modeling of the Microstructure Evolution during Metal Additive Manufacturing. *Comput. Mater. Sci.* **2018**, *141*, 207–220. [CrossRef]
23. Song, B.; Zhao, X.; Li, S.; Han, C.; Wei, Q.; Wen, S.; Liu, J.; Shi, Y. Differences in Microstructure and Properties between Selective Laser Melting and Traditional Manufacturing for Fabrication of Metal Parts: A Review. *Front. Mech. Eng.* **2015**, *10*, 111–125. [CrossRef]
24. Carroll, B.E.; Palmer, T.A.; Beese, A.M. Anisotropic Tensile Behavior of Ti–6Al–4V Components Fabricated with Directed Energy Deposition Additive Manufacturing. *Acta Mater.* **2015**, *87*, 309–320. [CrossRef]
25. Brandt, M. *Laser Additive Manufacturing: Materials, Design, Technologies, and Applications*; Woodhead Publishing: Cambridge, UK, 2016; ISBN 978-0-08-100434-0.
26. Boban, J.; Puthanveettil Madathil, A.; Ahmed, A.; Rahman, A. An Overview on Post-Processing of Metal Additive Manufactured Components. In *Materials Science and Materials Engineering*; University of Strathclyde, Glasgow: Glasgow, UK, 2024. Available online: https://www.sciencedirect.com/science/article/abs/pii/B9780323960205002417 (accessed on 14 April 2024).
27. Basha, S.M.; Venkaiah, N.; Srivatsan, T.S.; Sankar, M.R. Post-Processing Techniques for Metal Additive Manufactured Products: Role and Contribution of Abrasive Media Assisted Finishing. *Mater. Manuf. Process.* **2024**, *39*, 737–760. [CrossRef]
28. Actual State-of-the-Art of Electron Beam Powder Bed Fusion. Available online: https://www.tandfonline.com/doi/epdf/10.1080/26889277.2022.2040342?needAccess=true (accessed on 14 April 2024).
29. Körner, C. Additive Manufacturing of Metallic Components by Selective Electron Beam Melting—A Review. *Int. Mater. Rev.* **2016**, *61*, 361–377. [CrossRef]
30. Zhang, L.-C.; Liu, Y.; Li, S.; Hao, Y. Additive Manufacturing of Titanium Alloys by Electron Beam Melting: A Review. *Adv. Eng. Mater.* **2018**, *20*, 1700842. [CrossRef]
31. Galati, M. Chapter 8—Electron Beam Melting Process: A General Overview. In *Additive Manufacturing*; Pou, J., Riveiro, A., Davim, J.P., Eds.; Handbooks in Advanced Manufacturing; Elsevier: Amsterdam, The Netherlands, 2021; pp. 277–301, ISBN 978-0-12-818411-0.
32. Raghavan, N.; Simunovic, S.; Dehoff, R.; Plotkowski, A.; Turner, J.; Kirka, M.; Babu, S. Localized Melt-Scan Strategy for Site Specific Control of Grain Size and Primary Dendrite Arm Spacing in Electron Beam Additive Manufacturing. *Acta Mater.* **2017**, *140*, 375–387. [CrossRef]
33. Sames, W.J.; Unocic, K.A.; Dehoff, R.R.; Lolla, T.; Babu, S.S. Thermal Effects on Microstructural Heterogeneity of Inconel 718 Materials Fabricated by Electron Beam Melting. *J. Mater. Res.* **2014**, *29*, 1920–1930. [CrossRef]
34. Dehoff, R.R.; Kirka, M.M.; List, F.A.; Unocic, K.A.; Sames, W.J. Crystallographic Texture Engineering through Novel Melt Strategies via Electron Beam Melting: Inconel 718. *Mater. Sci. Technol.* **2015**, *31*, 939–944. [CrossRef]
35. Sun, S.-H.; Koizumi, Y.; Saito, T.; Yamanaka, K.; Li, Y.-P.; Cui, Y.; Chiba, A. Electron Beam Additive Manufacturing of Inconel 718 Alloy Rods: Impact of Build Direction on Microstructure and High-Temperature Tensile Properties. *Addit. Manuf.* **2018**, *23*, 457–470. [CrossRef]
36. Kirka, M.M.; Medina, F.; Dehoff, R.; Okello, A. Mechanical Behavior of Post-Processed Inconel 718 Manufactured through the Electron Beam Melting Process. *Mater. Sci. Eng. A* **2017**, *680*, 338–346. [CrossRef]
37. Strondl, A.; Palm, M.; Gnauk, J.; Frommeyer, G. Microstructure and Mechanical Properties of Nickel Based Superalloy IN718 Produced by Rapid Prototyping with Electron Beam Melting (EBM). *Mater. Sci. Technol.* **2011**, *27*, 876–883. [CrossRef]
38. Helmer, H.E.; Körner, C.; Singer, R.F. Additive Manufacturing of Nickel-Based Superalloy Inconel 718 by Selective Electron Beam Melting: Processing Window and Microstructure. *J. Mater. Res.* **2014**, *29*, 1987–1996. [CrossRef]
39. Karimi, P.; Sadeghi, E.; Ålgårdh, J.; Olsson, J.; Colliander, M.H.; Harlin, P.; Toyserkani, E.; Andersson, J. Tailored Grain Morphology via a Unique Melting Strategy in Electron Beam-Powder Bed Fusion. *Mater. Sci. Eng. A* **2021**, *824*, 141820. [CrossRef]
40. Helmer, H.; Bauereiß, A.; Singer, R.F.; Körner, C. Grain Structure Evolution in Inconel 718 during Selective Electron Beam Melting. *Mater. Sci. Eng. A* **2016**, *668*, 180–187. [CrossRef]
41. Ding, X.; Koizumi, Y.; Aoyagi, K.; Kii, T.; Sasaki, N.; Hayasaka, Y.; Yamanaka, K.; Chiba, A. Microstructural Control of Alloy 718 Fabricated by Electron Beam Melting with Expanded Processing Window by Adaptive Offset Method. *Mater. Sci. Eng. A* **2019**, *764*, 138058. [CrossRef]
42. Dehoff, R.R.; Kirka, M.M.; Sames, W.J.; Bilheux, H.; Tremsin, A.S.; Lowe, L.E.; Babu, S.S. Site Specific Control of Crystallographic Grain Orientation through Electron Beam Additive Manufacturing. *Mater. Sci. Technol.* **2015**, *31*, 931–938. [CrossRef]
43. Polonsky, A.T.; Raghavan, N.; Echlin, M.P.; Kirka, M.M.; Dehoff, R.R.; Pollock, T.M. Scan Strategies in EBM-Printed IN718 and the Physics of Bulk 3D Microstructure Development. *Mater. Charact.* **2022**, *190*, 112043. [CrossRef]
44. Boettinger, W.J.; Coriell, S.R.; Greer, A.L.; Karma, A.; Kurz, W.; Rappaz, M.; Trivedi, R. Solidification Microstructures: Recent Developments, Future Directions. *Acta Mater.* **2000**, *48*, 43–70. [CrossRef]

45. Lee, Y.S.; Kirka, M.M.; Dinwiddie, R.B.; Raghavan, N.; Turner, J.; Dehoff, R.R.; Babu, S.S. Role of Scan Strategies on Thermal Gradient and Solidification Rate in Electron Beam Powder Bed Fusion. *Addit. Manuf.* **2018**, *22*, 516–527. [CrossRef]
46. Knapp, G.L.; Raghavan, N.; Plotkowski, A.; DebRoy, T. Experiments and Simulations on Solidification Microstructure for Inconel 718 in Powder Bed Fusion Electron Beam Additive Manufacturing. *Addit. Manuf.* **2019**, *25*, 511–521. [CrossRef]
47. Ramakrishnan, P. Welding Metallurgy. *Indian Weld. J.* **1972**, *4*, 89. [CrossRef]